Journal of Sound and Vibration 329 (2010) 786–803

Contents lists available at ScienceDirect

Journal of Sound and Vibration

journal homepage: www.elsevier.com/locate/jsvi

Turbulence and heat excited noise sources in single and coaxial jets

Seong Ryong Koh *, Wolfgang Schröder, Matthias Meinke

Institute of Aerodynamics, RWTH Aachen University, Wüllnerstraße 5a, 52062 Aachen, Germany

ARTICLE INFO

Article history:
Received 10 June 2008
Received in revised form
16 August 2009
Accepted 7 October 2009
Handling Editor: M.P. Cartmell
Available online 5 November 2009

ABSTRACT

The generation of noise in subsonic high Reynolds number single and coaxial turbulent jets is analyzed by a hybrid method. The computational approach is based on large-eddy simulations (LES) and solutions of the acoustic perturbation equations (APE). The method is used to investigate the acoustic fields of one isothermal single stream jet at a Mach number 0.9 and a Reynolds number 400,000 based on the nozzle diameter and two coaxial jets whose Mach number and Reynolds number based on the secondary jet match the values of the single jet. One coaxial jet configuration possesses a cold primary flow, whereas the other configuration has a hot primary jet. Thus, the configurations allow in a first step the analysis of the relationship of the flow and acoustic fields of a single and a cold coaxial jet and in a second step the investigation of the differences of the fluid mechanics and aeroacoustics of cold and hot coaxial jets. For the isothermal single jet the present hybrid acoustic computation shows convincing agreement with the direct acoustic simulation based on large-eddy simulations. The analysis of the acoustic field of the coaxial jets focuses on two noise sources, the Lamb vector fluctuations and the entropy sources of the APE equations. The power spectral density (PSD) distributions evidence the Lamb vector fluctuations to represent the major acoustic sources of the isothermal jet. Especially the typical downstream and sideline acoustic generations occur on a cone-like surface being wrapped around the end of the potential core. Furthermore, when the coaxial jet possesses a hot primary jet, the acoustic core being characterized by the entropy source terms increases the low frequency acoustics by up to 5 dB, i.e., the sideline acoustics is enhanced by the pronounced temperature gradient.

1. Introduction

High speed jets from aircraft engines generate intensive noise, which is produced by the turbulent mixing of the jet with the ambient fluid. Although the early investigations of jet noise go back to Lighthill in the 1950s [1,2], there are still numerous open questions to jet noise especially when technologically relevant configurations such as coaxial jets are considered. For this reason, noise generation mechanisms of coaxial jet configurations are investigated in this paper. To parallel with the acoustic effect of multiple shear layers an isothermal single jet is also discussed.

Since 1952 a vast number of publications has appeared on jet noise generated by turbulence interacting with shear layers, Mach wave radiation, and convecting vortex packets [3]. One of the main issues was to reveal near-field turbulent structures which characterize the far-field downstream acoustic radiation. This question has motivated the huge accumulation of numerical and experimental researches. In his brilliant acoustic analogy Lighthill introduced the source

* Corresponding author. Tel.: +49 241 80 90400; fax: +49 241 80 92257.
E-mail address: s.koh@aia.rwth-aachen.de (S.R. Koh).

0022-460X/$ - see front matter © 2009 Elsevier Ltd. All rights reserved.
doi:10.1016/j.jsv.2009.10.012

concept to understand aerodynamically generated sound, e.g., quadrupole sound emission from turbulent flows. Assuming isotropic turbulence Proudman [4] showed the acoustic power to be characterized by the turbulent Mach number and the integral turbulent scale. Based on an analytic approach Lilley [5] presented the nonlinear acoustic variables involved in acoustic convection and refraction. The progress in sound radiation measurements led to a more detailed analysis of the jet noise spectra. Using the experimental evidence Tester and Morfey [6] developed a jet noise model based on Lilley's equation over a wide velocity and density range.

To understand the noise generation mechanism measured acoustic data from various jet configurations were used. Besides the far-field acoustic spectra the experimental investigations focused on the near field turbulent structures to identify the noise sources. Laufer et al. [7] found two distinct acoustic contributions which caused the Mach waves from the upstream mixing layer and the omni-directional radiation from the downstream of the potential core. In recent experimental studies Panda and Seasholtz [8] investigated jets at Mach numbers 0.95, 1.4, and 1.8 to locate noise sources in unheated turbulent flows. Using the laser-induced Rayleigh scattering technique, the detailed analysis evidenced that the correlation between the far-field acoustic pressure and the density fluctuations is a strong function of the polar angle. Concerning density inhomogeneity the experimental evidences by Viswanathan [9] indicate the acoustic change at high jet temperatures, which is an extra dipole source in the classical theories, to be caused by Reynolds number effects. A sound generation mechanism is proposed to have similarity spectra for the two components of turbulent mixing [10], i.e., the sound spectrum is dominated by the large turbulence structures and the fine-scale turbulence inside jets.

Accompanied with progress of high performance computation many numerical studies also appeared. For instance, Freund [11] used Lighthill's acoustic source term to understand the fundamental downstream radiation via an acoustic field synthesized with filtered acoustic source. Concerning the downstream and sideline acoustic radiation Bogey and Bailly [12] presented the detailed sound spectra of a high Reynolds number single jet based on a direct acoustic approach using large-eddy simulations. More recently, Spalart et al. [13] performed large-eddy simulations of jets to locate the sound sources in a specific frequency band and directivity. For the acoustic analysis the Ffowcs Williams–Hawkings integral formulation [14] was used to express the effect of extra sources on the acoustic transmission in turbulent mixing layers.

Each analysis in the literature shows the acoustic origin in the shear layer to be the velocity difference between the high momentum jet and the ambient flow. In the context of isothermal jets the vortical motion of turbulent eddies is the most significant noise source. In the theory of vortex sound [15] this source is denoted as the Lamb vector. To know the details of this vortex sound source as to the jet noise mechanism, it requires a deep understanding of turbulent motion, which is highly intricate in multiple shear layer flows. Therefore, to understand turbulent source mechanisms in multiple shear layers and to tackle the problem of analyzing sound generation in coaxial jets it is a reasonable approach to relate the investigation of coaxial flow and sound fields to a single jet reference case.

In an isothermal coaxial jet configuration at ambient temperature for the primary and secondary jet, the main acoustic source is determined by the turbulent shear layers between these streams. Morfey and Tester [16] discussed the attenuation of sound, scattering of noise by turbulent shear layers, and near field refraction by simplified models with vortex sheet and geometric acoustics. The noise reduction of shock-free coaxial jets was assessed by Tanna [17] on the basis of experimental data for normal- and inverted-velocity profiles. The major results were that the normal-velocity profile, i.e., the primary jet velocity is higher than the secondary jet velocity, always generated a louder acoustic field than the fully mixed equivalent single jet and that the effects of inverted-velocity profiles are independent from the effects of inverted-temperature profiles. The coaxial jet noise caused by the flow–acoustic interaction and by the changes in the source strength was more detailed by Tanna and Morris [18]. They concluded that the velocity ratio is a much more significant factor than the temperature ratio. Using the measured noise spectra of supersonic coaxial jets Dahl and Papamoschou [19] analyzed jets at normal-velocity profiles and identified the instability waves which grow and decay in the inner and outer shear layer. More recently, detailed parametric studies were conducted on the effect of the primary-secondary velocity ratio on the shock-associated noise by Viswanathan [20]. Tam et al. [21] discovered a noise component which radiates sound primarily in the downstream direction. The corresponding acoustics involves large turbulence structures and shock cells in the primary shear layer which separates the secondary and the primary jet. In a theoretical analysis on isothermal supersonic coaxial jets Dahl and Morris [22] reconsidered Lighthill's acoustic analogy to contain acoustic contributions of a primary and a secondary stream. That is, the turbulence level, the jet thrust compensation, and the spectral contributions were investigated. Among these effects the turbulence level turned out to be the decisive factor for the acoustic power which is proportional to the fourth power of the turbulence intensity. Ko and Kwan [23] analyzed the initial region of coaxial jets to evidence an instability mode which dominates the growth or decay of vortical components. Based on the measurement of the initial region Fisher et al. [24] developed the noise prediction model of unheated coaxial jets using acoustic principles from single jets.

In the early experimental study by Cocking [25] it was shown that the coaxial jet of a normal-velocity profile is quieter than the equivalent single jet when the secondary-to-primary jet temperature ratio is $T_s/T_p > 1$. On the basis of the noise prediction model of unheated coaxial jets Fisher et al. [26] considered heated primary jets to extend the model to coaxial jet with a temperature gradient. They revealed the presence of a dipole source in the heated primary jet in addition to the quadrupole sources linked to isothermal flows. Dahl and Morris [27] applied the instability wave noise generation model to coaxial supersonic jets. They showed the effects of the velocity ratio, density ratio, and area ratio by considering these factors independently. The experiment by Murakami and Papamoschou [28] showed the relevance of thermal effects on noise generation. In a few papers, e.g., Shur et al. [29] and Papamoschou [30], the sound radiation from complex jet

configurations, i.e., normal-velocity profiles or inverted-velocity profiles plus pronounced temperature gradients between the primary and the secondary streams and vice versa were considered, could be predicted at a reasonable accuracy over the essential frequency range.

Under the sixth EU framework program new coaxial jet configurations were specified and numerically investigated the results of which were published in several papers. Andersson et al. [31] performed large-eddy simulations of a heated coaxial jet to understand coaxial jet noise by using turbulence statistics and far-field acoustic computations. Based on a spectral linear estimation Tinney et al. [32] exploited the experimental data to understand the turbulence structures in terms of noise generation. The more generic issue of coaxial jet noise was addressed by Gröschel et al. [33] who proposed a detailed acoustic mechanism which is expressed by the source terms of the acoustic perturbation equations. Recently, Bogey et al. [34] tried to improve the noise prediction of coaxial jets by defining a realistic turbulence condition at the nozzle exit.

Overall, it can be stated that compared to the vast number of publications on single jets less research has been done on coaxial jets. The main aspects of coaxial jet noise mechanisms, where the velocity profile has the dominant effect, have been primarily observed on subsonic/supersonic dual streams. As to the hot coaxial jets it can be summarized that the impact of the velocity difference between the primary and secondary stream and of the temperature gradient has been described but not analyzed in detail as far as the acoustic sources are concerned. Thus, more systematic investigations are required to reveal the acoustic differences between single and coaxial jets and to identify the noise sources of multiple shear layers. Moreover, it is clear that for hot coaxial jets further research on the additional noise mechanisms and the corresponding sources and their impact on the sound field is necessary. This can be achieved when the identification of the major acoustic sources in coaxial jets and the understanding of the noise mechanism are more straightforward based on a set of equations containing terms, which are related to noise generation mechanisms, i.e., when some kind of direct mechanism–source relationship exists. This approach will be pursued in this study.

For this reason, coaxial jets are numerically investigated in this paper. However, it is necessary to relate the results of the coaxial jets to single jet findings since single jet data are the basis for most jet noise investigations. Therefore, a cold single jet at a Mach number 0.9 and a Reynolds number based on the nozzle diameter 400,000 is analyzed. This solution will be used to locate the fundamental vortex sound source. Next, two coaxial jet configurations, which have a secondary stream identical to that of the single jet configuration, i.e., of the ambient temperature flow at jet Mach 0.9, are computed. One coaxial jet possesses a cold and the other coaxial jet a hot primary jet. The comparison of the cold coaxial and the cold single jet will show the impact of the additional shear layer on the flow field and on the sound field. The juxtaposition of the hot and cold coaxial jet data will evidence the impact of the temperature gradient on the flow and noise characteristics.

The paper is organized as follows. In Section 2 the computational methods to determine the flow and sound field are introduced. Section 3 is divided into two parts. In the first part, the analysis focuses on vortex sound. Then in the second part, the acoustic fields and the corresponding noise sources of the cold and hot coaxial jets emphasizing the impact of the temperature gradient are analyzed. Finally, a brief summary of the essential results is given.

2. Numerical method

2.1. Flow parameters

The basic flow configuration is a round single jet at a Mach number 0.9 and a Reynolds number Re_D of 400,000 based on the jet diameter D, the centerline velocity U, the density ρ, and the viscosity μ at the nozzle exit. At the nozzle exit the ambient temperature is prescribed, i.e., an isothermal single jet is considered. For the large-eddy simulation a mean velocity profile $\overline{u}$ defined by a hyperbolic tangent

$$\frac{\overline{u}}{U}=\frac{1}{2}\left(1+\tanh\frac{R-r}{2\delta_m}\right) \tag{1}$$

is imposed on the shear layer at the nozzle exit where R is the jet radius, r is the radial distance from the jet centerline, and δ_m is the momentum thickness approximated by $0.05R$. The corresponding density distribution is modeled by the Crocco–Buseman relation and the ideal gas relation [12]. In large scale experiments the turbulent boundary layer exiting the nozzle possesses a very small thickness and a small corresponding time scale. To resolve the small scale turbulence the computational costs become quite expensive. Since the present LES is based on an implicit subgrid (SGS) approach the quality of the numerical solution is limited by the grid resolution. Due to those facts Bogey and Bailly [12] specified a mean velocity profile and seeded turbulence using artificial instability modes. The present study adopts the same procedure to develop the turbulent jets.

The coaxial jets possess the same Reynolds number $\rho_s U_s D/\mu_s$ of 400,000 based on the mean velocity of the secondary jet U_s at the nozzle exit. The Mach number of the secondary stream is $U_s/a_\infty = 0.9$ and the temperature ratio of the secondary flow and the ambient fluid is $T_s/T_\infty = 1.0$ for both coaxial jet configurations. Furthermore, the ratio of secondary and primary flow diameter is alike for the cold and hot coaxial jets, $D_s = 2D_p$. The difference of the coaxial jets occurs in the temperature of the primary jet. The cold configuration possesses a temperature $T_p = T_\infty$, whereas the hot configuration has a primary jet temperature $T_p \simeq 2.7T_\infty$. That is, as to the discussion of the acoustic field vortex sound will be the major noise source in the cold configuration. When the hot coaxial jet will be analyzed, another source due to the temperature gradient

Table 1
Flow parameters and notation of the coaxial jets: cj_c (coaxial jet with cold primary flow), cj_h (coaxial jet with hot primary flow), subscript 'p' (primary jet), subscript 's' (secondary jet).

Condition	$\rho_s U_s D/\mu_s$	U_s/a_∞	T_s/T_∞	U_s/U_p	T_s/T_p	U_p/a_p	U_s/a_s
cj_c	400,000	0.9	1.0	0.9	1.0	1.0	0.9
cj_h	400,000	0.9	1.0	0.9	0.37	0.6	0.9

between the primary and secondary jets will come into play and will interact with the vortex generated noise. The notation and the flow parameters of the coaxial jets are summarized in Table 1.

2.2. Governing equations and computational approach

The governing equations of the flow field are the unsteady compressible Navier–Stokes equations being filtered using the Favre-averaging procedure. The system of equations is closed by an implicit eddy diffusivity approach [35]. The details of the general set-up of the large-eddy simulation (LES) method, the quality of which has been proven in several analyses [36–39], are given in Meinke et al. [40].

The equations describing the sound propagation are the acoustic perturbation equations (APE). Since a compressible flow problem is tackled the APE-4 system is used [41]. The APE formulation can be exactly derived from the viscous conservation equations by a filtering procedure in the Fourier/Laplace space. The filtering procedure ensures that only the acoustic modes are propagated by the resulting wave equation. Convection and refraction effects are taken into account in the higher order, i.e., nonlinear wave equation. In the final formulation the nonlinear terms containing entropy fluctuations occur as additional source terms on the right-hand side. Incorporating the entropy gradient terms and using the first-order formulation of the second law of thermodynamics the APE-4 system reads

$$\frac{\partial p'}{\partial t} + \overline{a}^2 \nabla \cdot \left(\overline{\rho}\mathbf{u}' + \overline{\mathbf{u}} \frac{p'}{\overline{a}^2} \right) = \overline{a}^2 q_c, \tag{2}$$

$$\frac{\partial \mathbf{u}'}{\partial t} + \nabla(\overline{\mathbf{u}} \cdot \mathbf{u}') + \nabla\left(\frac{p'}{\overline{\rho}}\right) = \mathbf{q}_m, \tag{3}$$

where the original forms of the right-hand side terms are

$$q_c = -\nabla \cdot (\rho'\mathbf{u}')' + \frac{\overline{\rho}}{c_p}\frac{\overline{D}s'}{Dt}, \tag{4}$$

$$\mathbf{q}_m = -(\boldsymbol{\omega} \times \mathbf{u})' + T'\nabla\overline{s} - s'\nabla\overline{T} - \left(\nabla\frac{(u')^2}{2}\right)' + \left(\frac{\nabla \cdot \underline{\tau}}{\rho}\right)'. \tag{5}$$

Note that the source terms are determined by the LES and as such are connected with the subgrid scale (SGS) modeling. However, it is beyond the scope of the current analysis to investigate the impact of various SGS models on the source distribution. The overall quality of the LES data will be discussed using either numerical or experimental findings from the literature whenever possible. In this study all source terms but the viscous source are included in the right-hand side of the momentum equation of the APE system, i.e., $\mathbf{q}_m^* = \mathbf{q}_m - (\nabla \cdot \underline{\tau}/\rho)'$. The perturbed density is determined by the perturbation pressure

$$p' - \overline{a}^2\rho' = \frac{\gamma\overline{p}}{c_p}s'. \tag{6}$$

The first step of the hybrid method is based on an LES for the turbulent jet flow to provide the data of the noise source terms. Then, the corresponding acoustic field is computed by solving the acoustic perturbation equations.

The LES is based on a finite-volume method, in which the inviscid fluxes are spatially discretized by the AUSM scheme with the MUSCL approach and a centered approximation for the pressure term. The viscous terms are approximated by a centered discretization. For the temporal integration an explicit five-step Runge–Kutta formulation is used. The numerical details are described in Meinke et al. [40]. To eliminate undesirable wave reflections on the boundaries, a sponge layer is imposed [42]. The mean inflow condition of the LES is modeled to have a hyperbolic tangent profile. To ensure a turbulent inflow distribution, an artificial forcing based on several azimuthal modes is used [12].

The numerical method for the acoustic simulations requires a high spatial resolution in the wavenumber space and a high temporal accuracy in the frequency domain. To accurately resolve the acoustic wave propagation, the seven-point stencil dispersion-relation preserving (DRP) scheme [43] is used for the spatial discretization and an alternating 5–6 stage low-dispersion and low-dissipation Runge–Kutta method for the temporal integration [44]. On the inner boundaries between the inhomogeneous and the homogeneous acoustic domain an artificial damping zone has been implemented to suppress spurious sound generated on the embedded boundaries of the LES and the acoustic domain [45]. A detailed

description of the two-step method and the discretization of the Navier–Stokes equations and the acoustic perturbation equations is given in Schröder et al. [46] in a general context and in Gröschel et al. [47] with respect to jet flows.

At transonic flows the discrepancy of the length scales between acoustic waves and near field turbulent flows is more or less negligible such that it could be conjectured an LES could be efficiently used for the direct prediction of the acoustic field in the source region. However, although the advantage supported by length-scale discrepancy arguments no longer holds, the hybrid approach is still appealing since tailor-made numerics for the flow field and the acoustic field can be used resulting in a highly efficient numerical method. Furthermore, Koh et al. [48] using an isothermal single jet configuration showed the two-step approach, based on sequentially solving the Navier–Stokes equations on a source resolving grid and the acoustic perturbation equations on an acoustic domain, to yield the same acoustic field as a direct acoustic simulation based on a pure solution of the Navier–Stokes equations on the entire computational domain.

2.3. Computational domain

In Fig. 1 the coordinate system and a schematic of the LES domain, which is denoted by the dotted line, and the acoustic propagation region, which is encompassed by the solid line, are presented. The vector **r** represents the distance from the z-coordinate and θ is an angular coordinate between the positive streamwise direction (z-coordinate) and the position vector $\mathbf{r}_p$ from the nozzle exit.

The LES domain extends $12.5D$ in the radial direction and $25D$ in the streamwise direction. To prevent the spurious wave reflection on the boundary the sponge zone is defined at $r>8D$ and $z>17.5D$. A traction free condition [49] is used on the radial boundaries. The numerical mesh is illustrated in Fig. 2. The total number of grid points in the LES domain is

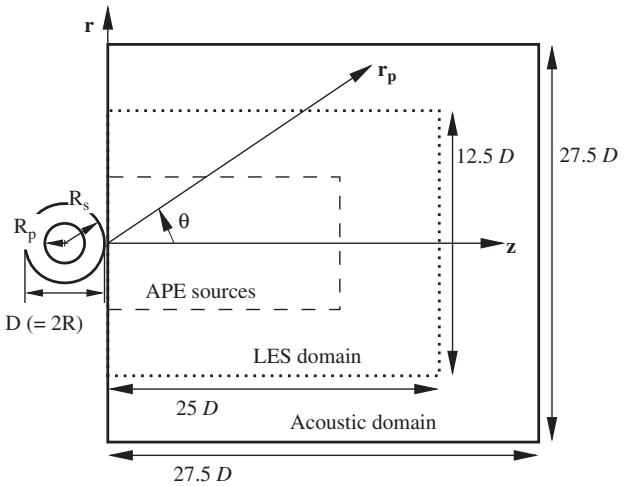

Fig. 1. Schematic of the computational domains in the r–z plane; ··· LES domain, — APE domain, – – – acoustic source region for APE, θ is the angle between the position vector $\mathbf{r}_p$ and the jet streamwise direction (z-coordinate), the single jet diameter is denoted by $D(=2R)$, R_p and R_s are the primary and secondary jet radii of the coaxial jet, respectively.

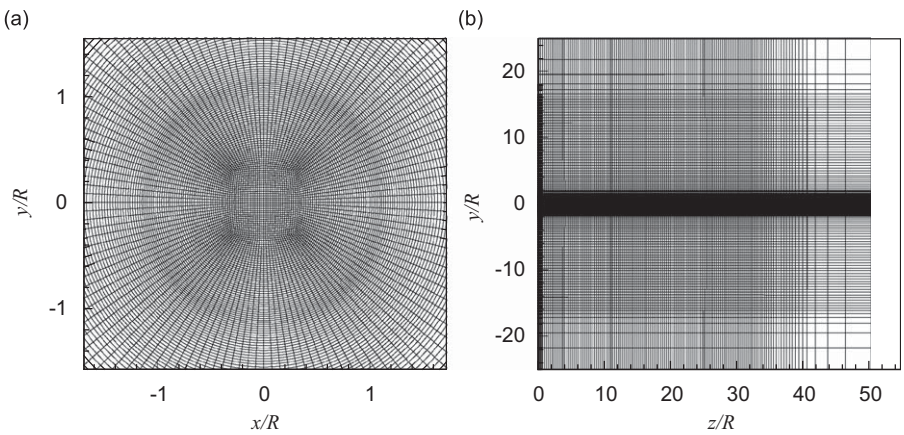

Fig. 2. Numerical mesh of LES, (a) jet inlet plane, (b) side-view at the $x=0$ plane (every 4th grid only).

20,142,144. In the axial direction the grid points are uniformly distributed in the region $z \leq 16D$ with $\Delta z = 0.035D$. The minimum grid spacing in the radial direction is $\Delta r_{MIN} = 0.01D$. This minimum grid spacing is gradually increased to reach $\Delta r = 0.05D$ at the location of $r = 8D$. Exactly the same mesh is used for the flow simulations of the single (denoted by 'sj') and the coaxial jets (denoted by 'cj_c' and 'cj_h'). That is, only the area where the inflow boundary condition is imposed is different.

During the flow simulation an inflow forcing technique is used to generate an artificial turbulent transition. At each end of time step an artificial vortex ring is imposed on each shear layer. The inflow forcing is controlled to generate proper turbulence with the grid size and the random azimuthal modes at the vortex ring. Note that in the present study, when an artificial velocity forcing is used to mimic the upstream turbulence intensity, the same grid resolution at the nozzle exit is chosen for numerical consistency when single and coaxial jets are investigated. That is, the various shear layers at single and coaxial jets are captured with the same grid resolution. Since the parameters involved in the artificial forcing do influence the jet development and hence the acoustics, the consistent numerical condition for the nozzle outflow is a must. A detailed discussion of the impact of the artificial forcing and the grid resolution at high Reynolds numbers on the flow and acoustic field can be found in [50].

The noise source region which is denoted by the dashed line in Fig. 1 extends $17.5D$ in the axial direction and $3D$ in the radial direction. The acoustic source terms calculated in this area used for the acoustic simulation. The acoustic perturbation equations are solved on a domain which is five times larger than the LES source region, i.e., it extends $27.5D$ in the axial and radial direction. Having a minimum spacing $\Delta r = 0.02D$ and a maximum spacing $\Delta r = 0.1D$ in the radial direction and a constant spacing in the axial direction of $\Delta z = 0.035D$ results in 12,359,952 cells to resolve the acoustic field. Based on the DRP scheme the spectral resolution in the wavenumber space requires at least six points per wavelength λ. Consequently, on the present acoustic mesh the maximum Strouhal number $St = fD/U$ is approximately $D/(\lambda_m U/a_\infty) \simeq 4.4$ where the mean wavelength λ_m is 5.5 times the maximum grid spacing of the acoustic domain.

3. Results

The discussion of the findings possesses the following structure. First, the vortex sound source is analyzed in detail considering its location and its impact on the acoustic field. The fundamental physics of single and coaxial jet flows is investigated by distributions of mean and turbulence quantities, i.e., the streamwise development of the mean velocity, the streamwise increase of the jet width, and the turbulence intensities on the jet centerline. Moreover, to locate the acoustic sources in the jets the power spectra of vortical sources are investigated.

Second, the hot and cold coaxial jet data are juxtaposed to evidence the impact of the temperature gradient on sound generation and propagation. Using the entropy sources of the APE-4 equations, the source strength inside a hot stream is analyzed by discrete Fourier transform. The findings will evidence the acoustic radiation to be intensified due to the pronounced temperature gradient. Finally, the spatial regions and the frequency band of the entropy source terms are shown and their relationship with the heat excited acoustics is discussed.

3.1. Vortex sound source

In the isothermal single jet the strong vortical motions in the turbulent shear layer generate the acoustic field. The major sound source is represented in the APE-4 system by the perturbed Lamb vector $\mathbf{L}'$ which is defined such as $(\boldsymbol{\omega} \times \mathbf{u})'$ in Eq. (5). Using the LES results under the realizability regime of turbulent flow the present statistical analysis defines in detail the turbulent distributions, which determine the temporal and spatial variations of the noise source. Moreover, the acoustic identification evidences the sound generation to be caused by convecting turbulence and nonlinear transition near the end of the potential core. First, the mean flow fields of the single and coaxial jet configurations are discussed and then, the acoustic field of the isothermal single jet is analyzed.

3.1.1. Mean flow field

In the following, the mean axial velocity profiles of the problems listed in Table 1 are compared, i.e., the development of the shear layer and the distribution of the turbulence intensities are considered. The sampling time period is $T_{sample} = 800R/U$ at a time step $\Delta t_{sample} = 0.5R/U$ such that 1600 LES snapshots are averaged. The findings are compared with the numerical data of the single jet configuration by Bogey and Bailly [12] and experimental findings by Zaman [51].

In Fig. 3(a) the axial profiles of the mean centerline velocity normalized by the primary nozzle exit velocity U_p show the flow development on the jet centerline. The length of the potential core of the isothermal single jet is $z \simeq 12R$. This length almost matches that of the cold coaxial jet, whereas the hot coaxial jet possesses due to the enhanced mixing process by the temperature gradient a much smaller extent of the potential core $z \simeq 8R$. The axial profile of the jet half-width in Fig. 3(b) also evidences the hot coaxial jet to start growing slightly more upstream though the jet spreading rate of the various jets is almost alike.

The axial distributions of the fluctuations of the axial velocity on the centerline are shown in Fig. 4(a). The comparison of the numerical single jet distributions with the experimental single jet data by Zaman [51], Arakeri et al. [52], and Ahuja et al. [53] shows a convincing agreement at $z \geq 7R$ especially with the Zaman findings. Downstream of an initial region the

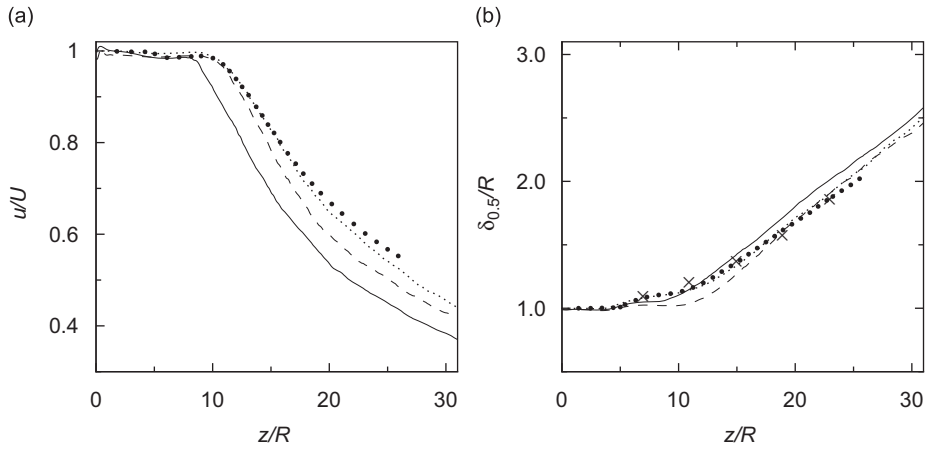

Fig. 3. Mean velocity profiles of the single and coaxial jets; (a) mean streamwise velocity on the jet centerline and (b) evolution of jet half-width $\delta_{0.5}/R_s$ as a function of the streamwise coordinate, — cj_h, – – – cj_c, ⋯ sj, • Bogey and Bailly [12], single jet, × experiment by Zaman [51], single jet.

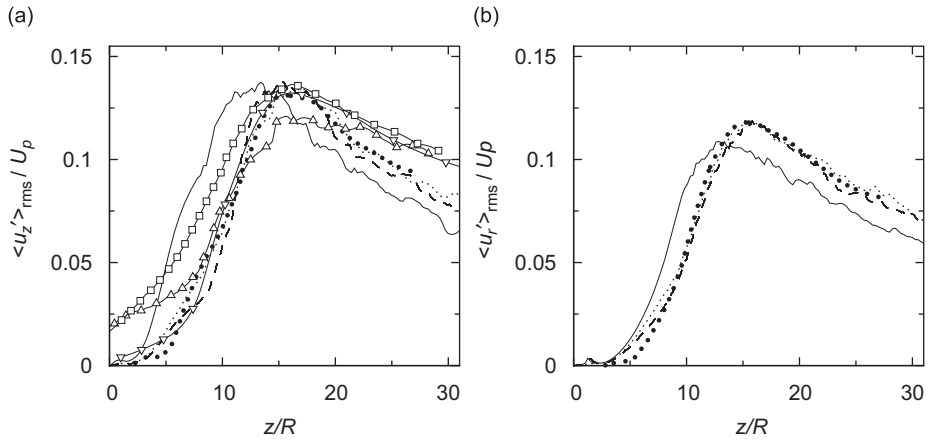

Fig. 4. Profiles of the (a) axial and (b) radial turbulence intensities on the jet centerline as a function of the streamwise coordinate, — cj_h, – – – cj_c, ⋯ sj, • single jet by Bogey and Bailly [12], ∇ experimental data by Zaman [51], △ experimental data by Arakeri et al. [52], □ $M_j = 0.78$ experimental data by Ahuja et al. [53].

fluctuations rise rapidly and peak slightly downstream of the end of the potential core. The hot coaxial jet reaches its maximum at $z \simeq 12R$, whereas the cold jets reach their maximum at $z \simeq 15R$. The nonlinear development is also observed in the axial distributions of the turbulence intensities of the radial velocity component in Fig. 4(b). Due to the rapid flow saturation the peak of the hot primary flow occurs at $u_{r,\mathrm{rms}}' \simeq 0.10U_p$ and that of the cold configurations at $u_{r,\mathrm{rms}}' \simeq 0.12U_p$. That is, the hot primary stream enhances the nonlinear transition process. Note, if the turbulence intensities are rescaled by the single jet $U_{p,sj}$, the rms values of the two coaxial jets are larger by a factor defined by the velocity ratio $U_{p,cj}/U_{p,sj} \simeq 1.1$ which matches the value of the primary-to-secondary velocity ratio of the coaxial jets.

In brief, the turbulent distributions of the single jet and the cold coaxial jet are almost identical although the actual fluctuation level differs by the ratio of the primary velocity $U_{p,cj}/U_{p,sj}$. The rapid mixing of the hot coaxial jet leads to a steep increase of the turbulence intensities near the end of the potential core, whereas downstream of the potential core slightly larger velocity fluctuations occur in the cold jets. Since it is well known that there is a close link between turbulence in the core region and the sound generation [2], it is conjectured that the effective sound sources inside the hot coaxial jet generate a more powerful acoustic field. The discussion on the primary-to-secondary velocity ratio was detailed by Tanna [17], Tanna and Morris [18] who addressed the greatly enhanced noise level by decreasing the velocity ratio $U_s/U_p < 1$. This issue will be tackled further below when the acoustic field of the hot coaxial jet will be considered. Next, the results of the statistical analysis and the impact of the turbulence structure on the overall acoustics of the single jet will be discussed.

3.1.2. Acoustics of an isothermal single jet

The isothermal single jet is the basic flow of the present aeroacoustics analysis. To validate the present hybrid numerics the acoustic field based on the APE-4 system is analyzed using the detailed sound spectra of LES data. In this section, we emphasize the significance of the Lamb vector fluctuations of Eq. (5) due to the isothermal jet condition.

Based on the LES solution of the core region, where the motion of the vortical structures determines the effective acoustic source, the near far-field acoustics is computed by the APE-4 system. The data processing for the acoustic simulation uses 3200 LES snapshots at a time step $\Delta t_{\text{sample}} = 0.1R/U$. The discrete source data are quadratically interpolated. The time step of the acoustic analysis $\Delta t_{\text{APE},sj}$ is $0.012R/a_\infty$ to ensure a stable solution. The acoustic computations are performed over a time period $T_{\text{APE},sj} = 320R/U$. During the time interval the acoustic waves initiated in the jet core region propagate a distance seven times larger than the maximum extent of the computational domain.

In Fig. 5(a) the acoustic field generated by the isothermal single jet is shown. In the core region the corresponding Lamb vector field is generated by the turbulent shear layers. The Lamb vector can be considered the vortex sound source which causes the strong acoustic radiation near the jet potential core. The time signals of the acoustic pressure at two locations are shown in Fig. 5(b). At the location 'P1' the short wave signals dominate, whereas at the location 'P2' low frequency waves are captured. The main characteristics of the stronger 'P2' distribution is caused by the jet development. This low-angle radiation is clearly different from the sideline acoustics in 'P1' where the high frequency contribution dominates.

In Fig. 6 the LES solution has the peak overall sound pressure level (OASPL) at about $12R$ downstream of the potential core, i.e., at $z = 24R$. The comparison with the experimental data by Barré et al. [54] shows on the one hand, the qualitative agreement of the distributions and on the other hand, a difference of 1–3 dB between the numerical and experimental data. This discrepancy is likely to be caused by the fact that in the LES the high wavenumber structures are not sufficiently described and therefore some damping mechanism is underpredicted. Furthermore, it has to be emphasized that the Reynolds number of the experiment was $Re_D \simeq 8 \times 10^5$, i.e., much higher than in the numerical analysis. When the current solutions are juxtaposed with the LES findings from Bogey and Bailly [12] a slight underprediction is observed since the mesh resolution in [12] is much coarser, i.e., by almost a factor of 20, than in the current computation. Nevertheless, the comparison between the direct LES and the hybrid LES/APE solutions shows the distribution to almost collapse. However, such a correspondence is only achieved if all the sources on the right-hand side of APE-4 system are taken into account.

The sound spectra at the axial locations $z = 12R$ and $z = 29R$ at the same radial distance $r = 15R$, i.e., at 'P1' and 'P2' given in Fig. 5, are presented in Fig. 7. The sampling rate of $0.1R/U$ suffices to resolve the maximum Strouhal number of 1.45. The pressure signal is determined to understand the characteristics of the near field acoustics. To be more precise, the sideline and the downstream noise propagation in Figs. 7(a) and (b) show a convincing agreement with the results of direct acoustic simulations by Bogey and Bailly [12]. The peak frequency of the present results occur at Strouhal number $fD/U \simeq 0.3$ for the downstream acoustics, which is associated with the turbulence entrainment from the shear layer mixing. The sideline noise at $z = 12R$ peaks at higher Strouhal number $fD/U \simeq 0.6$, which is induced by the flow instability of the shear layer.

The main concern of the present analysis is the identification of noise sources, which determine the acoustic field of the isothermal subsonic jet. To evidence the effective source the aerodynamic changes of turbulent eddies are detailed by using the spectral component. Instantaneous data are sampled over a period of $320R/U$ and are decomposed into 10 overlapping segments. Since the recorded signals are not periodic, the Hamming window function is used for all power spectra presented in this study. Note, a single isothermal jet configuration is analyzed and as such the dominant acoustic source is the Lamb vector fluctuation term in Eq. (5). Specifically, if the radial component of the Lamb vector fluctuations at a fixed radial position $L_r(r, m, z, t)$ is Fourier transformed in the z-direction as $\hat{L}_r(r, m, k, f)$, then the power spectral density is determined

$$\Phi_l(r, m, k, f) = \overline{\hat{L}_r(r, m, k, f)\hat{L}_r^*(r, m, k, f)}, \tag{7}$$

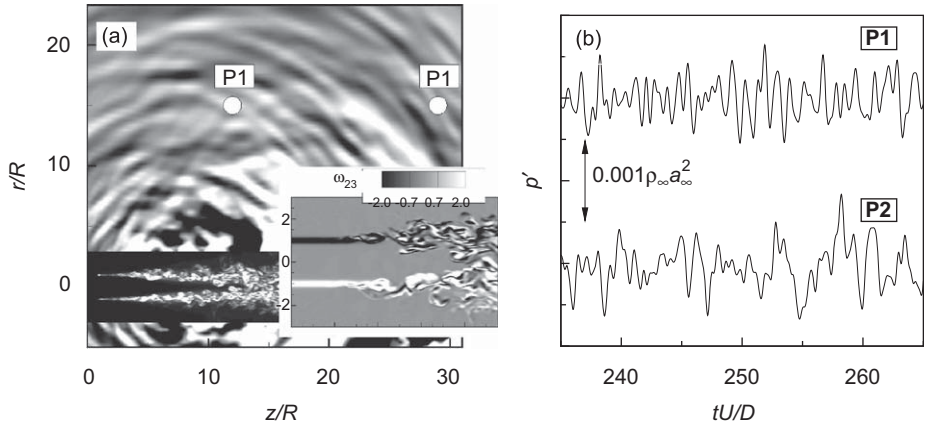

Fig. 5. Acoustic waves of the isothermal single jet predicted by the APE-4 system; (a) contours of the magnitude of the Lamb vector fluctuations ($|\mathbf{L}'| \leq 1.5a_\infty^2/R$), contours of a vorticity ($|\omega_{23} = \partial w/\partial y - \partial v/\partial z| \leq 2U/R$) and the acoustic pressure p' contour range ($|p'| \leq 5 \times 10^{-4}\rho_\infty a_\infty^2$), (b) acoustic pressure signals at the radial location $r = 15R$, P1 ($z = 12R$) for sideline acoustics and P2 ($z = 29R$) for downstream acoustics.

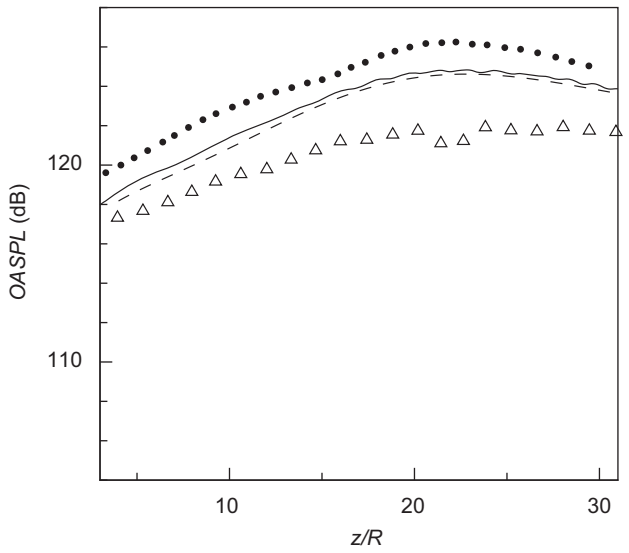

Fig. 6. Overall sound pressure level in dB at the radial distance of $r = 15R$ from the z-axis, — LES/APE, – – – LES, • single jet by Bogey and Bailly [12], △ experimental data by Barré et al. [54].

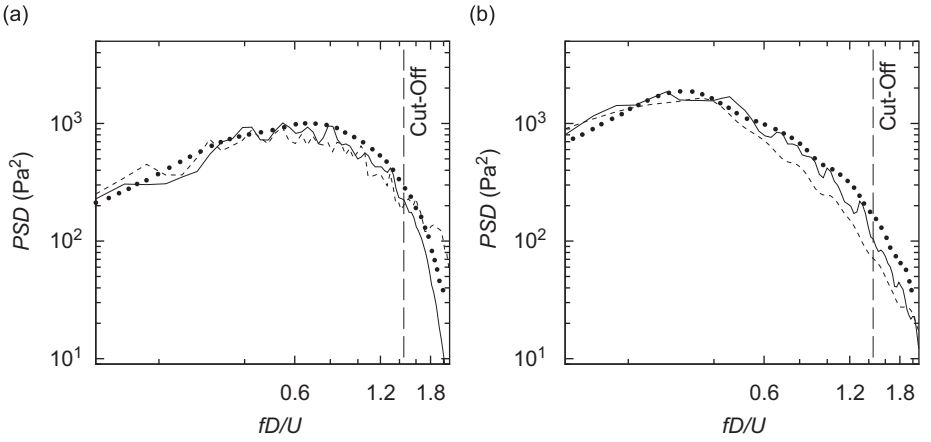

Fig. 7. Sound pressure spectrum at the circumferential location $r = 15R_s$, the cut-off frequency is located at $fD/U = 1.45$, (a) P1 ($z = 12R$), (b) P2 ($z = 29R$), — LES/APE, – – – LES, • LES by Bogey and Bailly [12], single jet.

where the overbar indicates the ensemble average, k is the wavenumber in the z-direction, * denotes a complex conjugate, and m means the m-th azimuthal mode.

The spectral distribution of $\Phi_l(r, m, k, f)$ has a realistic scale of turbulent eddy convection in a statistical sense. Therefore, the detection of the phase velocities in this power spectral density will yield the dominant turbulent scale in the frequency-wavenumber domain. Using a three-dimensional cylindrical domain the cross spectra with noise source convection can be determined. The cylindrical domain possesses a radius of $2D$ ($r \leq 2D$) and a length of $10D$ downstream of the nozzle exit ($0 \leq z \leq 10D$). The noise source signal is determined over the complete circumferential surface and is decomposed into the spectral component in a frequency-wavenumber space via Eq. (7). Finally, the power spectral density distribution is quantified by integrating the decomposed spectra over the surface. The details of this procedure can be found in the source filtering technique by Freund [11]. Fig. 8 shows the spectral distribution of the sound source $\mathbf{L}'$. The phase velocity of the noise source $M_c = -\omega/a_\infty k$ is defined by the wavenumber in the axial direction k and the angular frequency ω. The source distribution is confined to the phase velocity M_c of 0.5 which corresponds to a speed of $0.56U$.

The power spectra of the vortex sound source $\mathbf{L}'$ are shown in Fig. 9. The spectra of the radial component of the Lamb vector fluctuations are illustrated for three radial locations in a frequency(f)–space(z) plane. Near the jet centerline at $r = 0.1R$ in Fig. 9(a) the spectral peak of the Lamb vector fluctuations appears at the frequency $fD/U \simeq 0.4$, which is characteristic for downstream acoustics. The spectral density of the radial component of the Lamb vector fluctuations $\Phi_l(r, z, f)$ peaks at the axial location $z \simeq 15R$. It is clear from Fig. 9(b) that at $r = 0.5R$ the radial component of the power

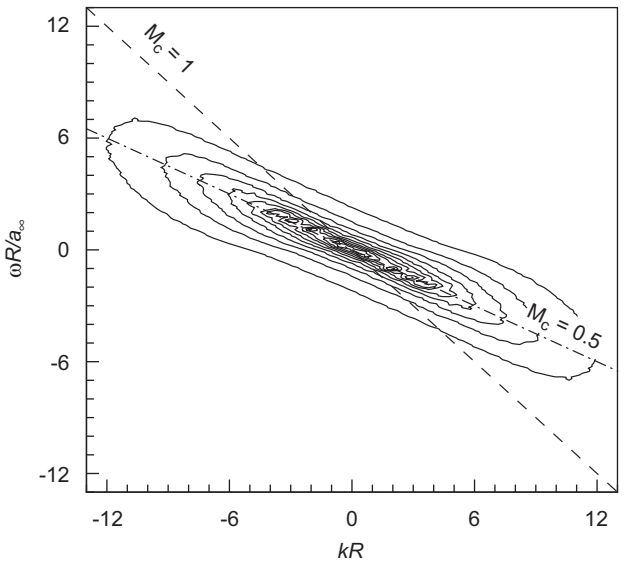

Fig. 8. Noise source spectrum in $\omega-k$ space, k is the wavenumber in the axial direction, ω is the angular frequency, $M_c=-\omega/a_\infty k$.

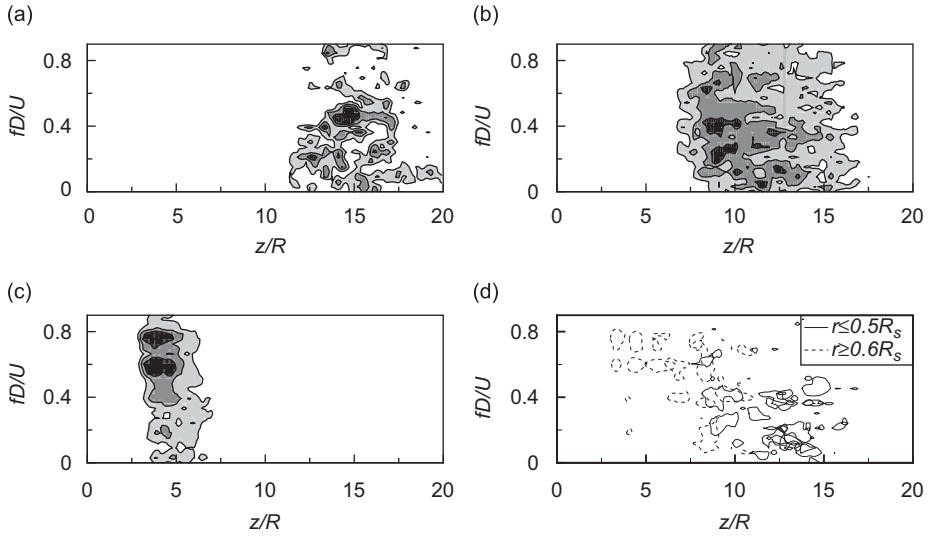

Fig. 9. Power spectral density (PSD) of the vortex sound source $\mathbf{L}'$ in an $f-z$ plane at several radii, (a) $r=0.1R$, (b) $r=0.5R$, (c) $r=R$, (d) $0.1R\leq r\leq R$, the levels of the non-dimensional spectral density $\Phi_l R^2U/a_\infty^4 D$ in the interval (a) and (b) [0.25, 0.4] and (c) [0.5, 0.8], (d) peak PSD regions at $0.1\leq r/R\leq 1$.

spectral density possesses a peak at an axial location $z=10R$. In the shear layer region at $r=R$, as shown in Fig. 9(c) based on the pronounced PSD regime, the spectral peak is located at the axial position at $z\simeq 5R$. Performing the same analysis in the range of $0.1\leq r/R\leq 1$ identifies the radial location of the noise sources determined by the radial component of the PSD in Fig. 9(d). Near the centerline the spectral peak is determined by the downstream acoustics at $fD/U=0.3\sim0.4$. Further off the centerline and closer to the shear layer at $r=R$, the spectral peak occurs at higher frequencies, i.e., it is characterized by sideline acoustics at $fD/U=0.6\sim0.8$.

In Fig. 10 contours of the turbulent kinetic energy and the Lamb vector fluctuations $\overline{L_r^2}$ are shown together with the peak locations of the power spectral density. To determine an effective source region, the local maxima of the Lamb vector fluctuations are defined on the $r-z$ coordinates where the spatial gradient $\partial\overline{L_r^2}/\partial r$ vanishes. The maximum value of the turbulent kinetic energy appears on the shear layer slightly upstream of the end of the potential core as shown in Fig. 10(a). The high-speed core entrains fluid via a pronounced shear layer where the turbulence production reaches a maximum. Unlike the distribution of the Lamb vector fluctuation in Fig. 10(b) the maxima of the turbulent kinetic energy appear to be parallel to the main flow direction. The Lamb vector fluctuations immediately reach their maximum values in the transition region of the shear layer. Spatially the maxima form a cone-shape surface covering the potential core. Downstream of the

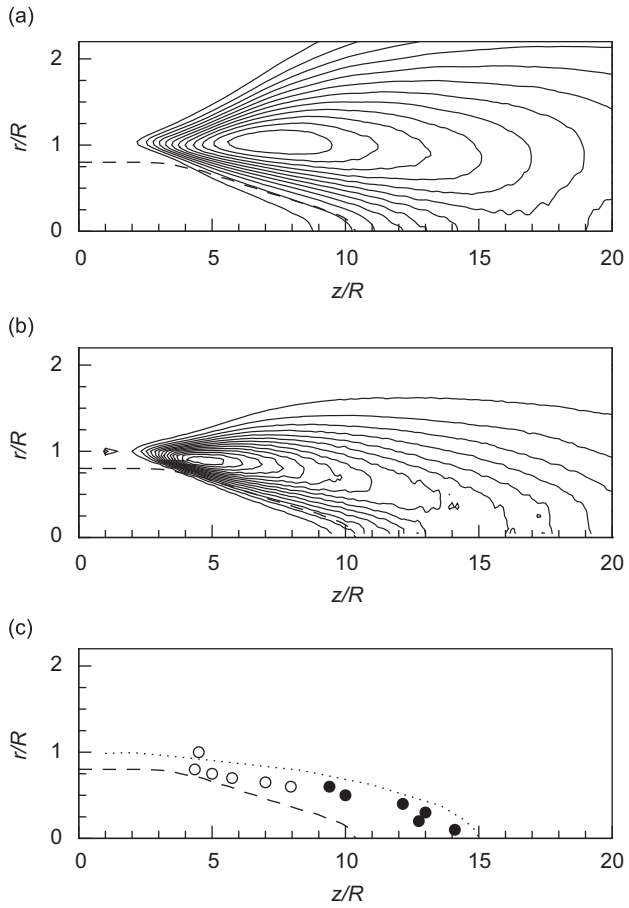

Fig. 10. Contours of turbulent kinetic energy, Lamb vector fluctuations in mean square values, and peak locations of power spectral density (PSD) of the Lamb vector fluctuations in the single jet, (a) turbulent kinetic energy, (b) Lamb vector fluctuations, (c) spectral peak: – – – potential core surface, ··· maxima of radial component of Lamb vector fluctuations, • peak locations of the PSD at $0.1 \leq r/R_s \leq 1$.

potential core the acoustics theory of isotropic turbulence [4] supports the jet noise mechanism determined by the motion of convecting turbulence which generates sound by compressing and expanding small fluid volumina. The comparison of the distributions of the maxima of the radial component of the Lamb vector fluctuations and the peak locations of the power spectral density in Fig. 10(c) shows a clear correspondence. That is, although the source spectrum also includes non-radiating parts, the coincidence with the distribution of the Lamb vector maxima evidences the immediate connection with the generation of noise near the end of the potential core. This result confirms the finding of Tucker [55] and Avital et al. [56] that the maximum of the subsonic sound source occurs just downstream of the potential core. The present source spectra illustrate clearly the signature of the dominant acoustic source induced by the mixing of the turbulent shear layer.

3.2. Hot vs. cold coaxial jets

The jets of coaxial nozzles provoke noise generation components radiating quite intensified acoustics. In this section, the overall acoustic fields of cold and hot coaxial jets are juxtaposed to emphasize heat-induced noise which is discussed at length using spectral analyses. The power spectra of the near far-field acoustics confirm the significance of the sources, which are excited by the turbulent stresses and the temperature gradient in the coaxial jets. Then, to especially analyze the impact of the hot fluid, the entropy terms of the APE-4 equations occurring in the primary jet are discussed.

3.2.1. Near field sources and acoustics of coaxial jets

Analogous to the single jet analysis the computation of the acoustic field of the coaxial jets is based on the source time interval $T_{\mathrm{APE},cj} = 320R_s/U_s$ of the LES solutions. For numerical stability the time step to solve the APE system $\Delta t_{\mathrm{APE},cj}$ is $0.011R_s/a_\infty$.

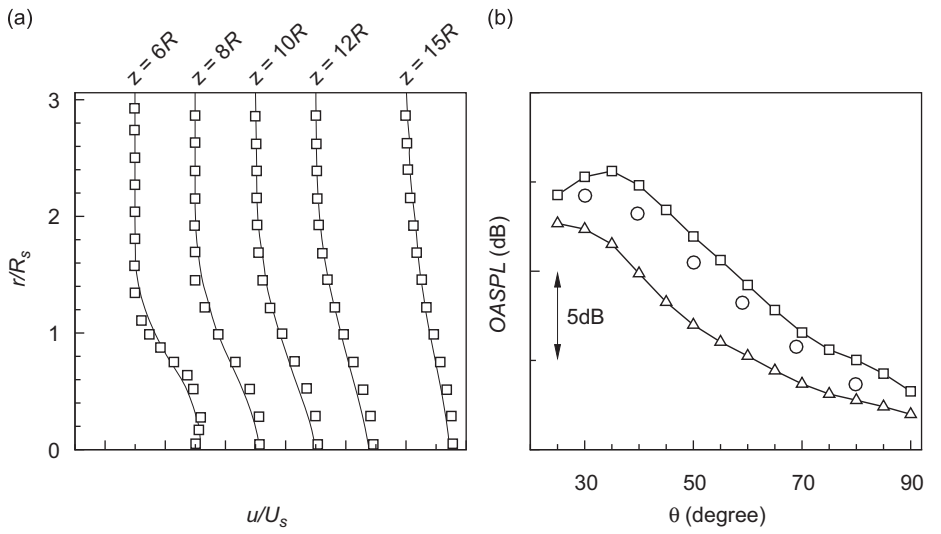

Fig. 11. Comparison of the LES/APE solution with experimental data, (a) mean axial velocity at several axial locations, □ experimental data [57], — LES, (b) ◦ experimental data [57], □ LES/APE 'cj_h' , Lamb vector + entropy term, △ LES/APE 'cj_h' , Lamb vector only.

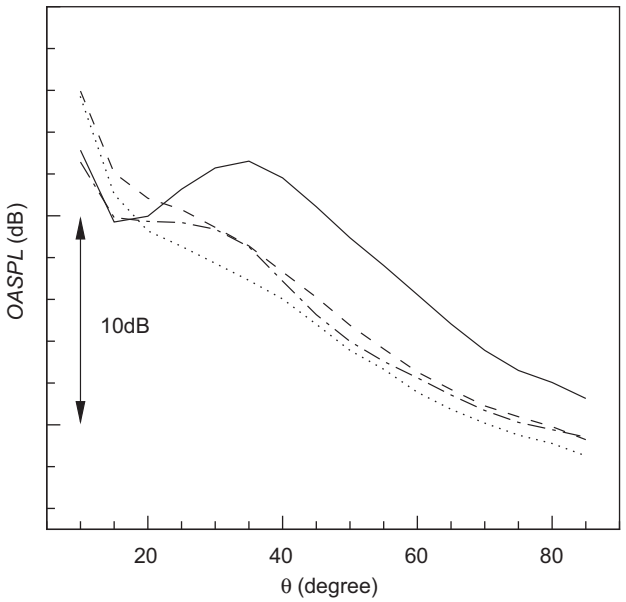

Fig. 12. Overall acoustic directivity based on the APE-4 system at $r_p = 40R_s$: — cj_h, – · – cj_h with Lamb vector only, – – – cj_c, ⋯ sj.

In Fig. 11 the experimental distributions of the mean axial velocity and the overall sound pressure level from [57] are compared with the LES/APE solutions. The comparison shows a convincing agreement of the LES results and the experimental data in Fig. 11(a). Fig. 11(b) emphasizes the impact of the temperature excited entropy sources on the OASPL. When only the Lamb vector is used as source term for the acoustic field a discrepancy is observed between the numerical and experimental distribution. This difference which is a function of the angle θ becomes much smaller, i.e., less than 3 dB, when the numerically simulated field is excited by the Lamb vector and the entropy sources. Furthermore, it is evident from Fig. 11(b) that the entropy terms, i.e., the temperature gradient, do have a pronounced influence especially for the acoustics within the angular range of $30^\circ \leq \theta \leq 70^\circ$.

In Fig. 12 the acoustic directivities at $r_p = 40R_s$ show a unique pattern for the hot coaxial jet acoustics. The maximum OASPL occurs at $\theta \simeq 35^\circ$ from the jet axis. Compared with the findings of the single and the cold coaxial jet the axial profile of the hot coaxial jet shows an approximately 5 dB higher acoustic pressure. Considering the small difference of 1–2 dB between the single and the cold coaxial jet, it can be conjectured that the hot primary jet excites another major sound source yielding a more powerful acoustic energy over a wide frequency range. This second major source is caused by the

heat content of the hot primary jet. Note, when the acoustic field of the hot coaxial jet is determined only by the vortex sound source ($\mathbf{L}'$) its overall acoustic directivity almost coincides with that of the cold coaxial jet. In other words, the vortex sound source is hardly impacted by the entropy source which makes the difference between the hot coaxial jet and the cold coaxial jet.

In Fig. 13 the acoustic spectra of the cold and the hot coaxial jets are compared. The sound pressure is determined at the radial distance $r_p = 40R_s$ from the jet axis with an angular increment of 5°. The acoustics of the cold coaxial jet in Fig. 13(a) shows the pronounced low frequency radiation at $\theta \leq 45°$. At higher angles rather flat sound spectra are observed up to a Strouhal number of $fD_s/U_s \simeq 0.6$. In Fig. 13(b) the acoustics of the hot coaxial jet is presented. Due to the heat impact of the temperature gradient on the noise generation the acoustic radiation at high angles is more intensified than that of the cold coaxial jet. The acoustic increment at the high angles is more confined to a low frequency band. That is, the heat excited acoustics corroborates the effects of an inhomogeneous density field as being discussed by Morfey [58] and also predicted by the analytical solution for hot jets by Lilley [59]. In the APE-4 system the acoustic source terms of Eqs. (4) and (5) contain the heat effects on the acoustic field. Concerning the downstream acoustics the spectral peak moves to the Strouhal number 0.5 for the hot coaxial jet against a Strouhal number 0.3 of the cold coaxial jet. This acoustic behavior is caused by the pronounced temperature gradient in the primary shear layer, which enhances the high frequency oscillations. Note, however, the present coaxial jet configurations have a mean inlet velocity distribution plus an artificial inflow forcing. This artificial excitation has to be kept in mind when the quantitative not the qualitative findings are considered. In Figs. 13(c) and (d) the current numerical results are compared with experimental data of Tanna and Morris [18]. The temperature ratio in the measurements was $T_s/T_p = 1$ and 0.5 and the velocity ratio was $U_s/U_p = 0.7$. The comparison is to be considered on a qualitative basis of the sound spectra since the details of the experimental jet configuration are different from the present numerical simulation. Over the frequency range ($fD/U_s \leq 1.2$) the numerical results qualitatively coincide with the measured data [18]. That is, the experimental findings confirm the numerical result that the downstream acoustic generation is enhanced due to the pronounced temperature gradient.

The acoustic directivity patterns of the cold and hot coaxial jets are presented in Fig. 14 for two Strouhal numbers at $fD_s/U_s = 0.3$ and 0.5. For the hot coaxial jet the low frequency acoustics (Fig. 14(a)) is more omni-directional than the high

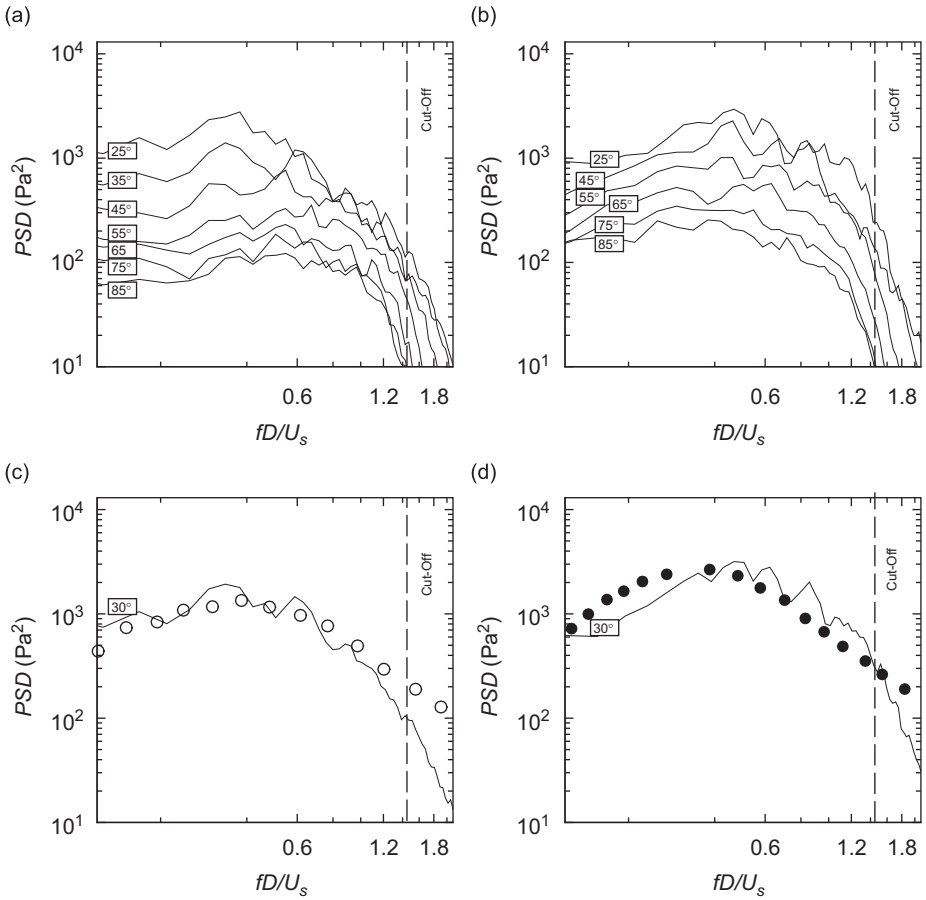

Fig. 13. Sound spectra of acoustic radiations at angles $25° \leq \theta \leq 85°$ at a distance $r_p = 40R_s$, (a) and (c) cold coaxial jet (cj_c), (b) and (d) hot coaxial jet (cj_h), experimental data [18], ◦ $U_s/U_p = 0.7, T_s/T_p = 1.0$, • $U_s/U_p = 0.7, T_s/T_p = 0.5$, the level of the experimental data is shifted for comparison.

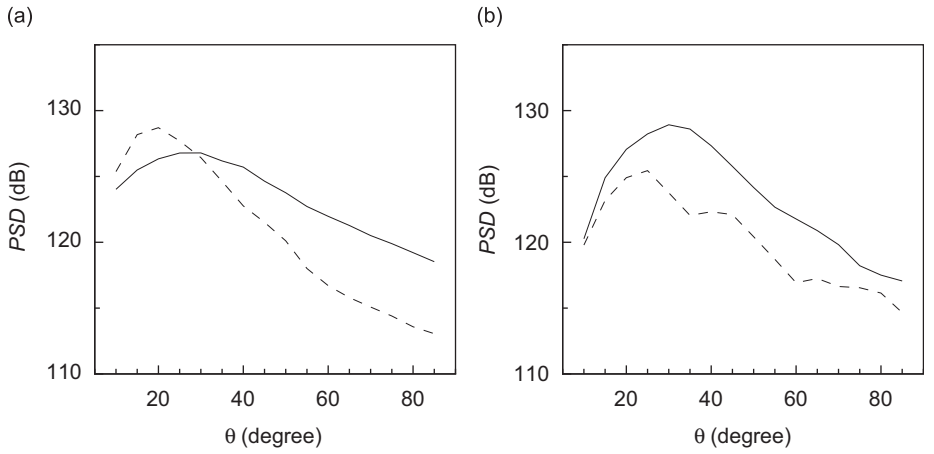

Fig. 14. Comparison of the acoustic directivity for two Strouhal numbers at $r_p = 40R_s$, (a) $fD_s/U_s = 0.3$, (b) $fD_s/U_s = 0.5$: — cj_h, – – – cj_c.

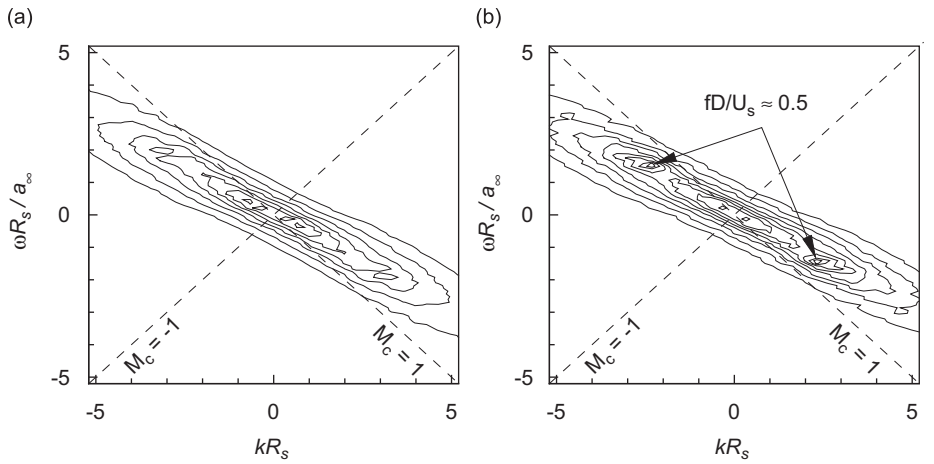

Fig. 15. Cross-spectral density distributions of the vortex source in the coaxial jets, (a) cold coaxial jet (cj_c), (b) hot coaxial jet (cj_h).

frequency acoustics (Fig. 14(b)). In the cold coaxial jet this frequency dependence is not as pronounced as in the hot coaxial jet. That is, the louder acoustic radiation at an angle of approximately 30° is not only due to the turbulent mixing of hot fluid but also due to the change of the sound speed between the shear layer developed by the temperature gradient. This result is more evident at $fD_s/U_s = 0.5$ than at $fD_s/U_s = 0.3$. Due to the temperature difference between the primary and the secondary stream the waves propagate through flow fields at varying sound speed. They are refracted to form a high angle acoustic radiation. The downstream acoustics of the hot coaxial jet is dominated by the high frequency component. Besides, the intense temperature gradient on the primary shear layer excites noise which is not observed in the cold coaxial jet. The heated flow contribution to the sideline acoustics, i.e., at $\theta \geq 60^\circ$, is evidenced in Fig. 14(a) for low frequency sound at $fD_s/U_s = 0.3$. The maximum increase of the sound level is about 5 dB.

The refraction in the hot coaxial jet indicates a deviation due to the acoustic effect of the mean temperature distribution which varies the speed of sound. Of course, this is not the only refraction source since there is also wave refraction due to the shear layer as has been investigated, e.g., by Tester and Morfey [6], Morfey and Tester [16]. The impact of the temperature gradient on the directivity of the sound field has been studied for a generic test problem in [60]. In this study, it has been shown that the temperature gradient driven refraction is more pronounced at higher angles. This conclusion is corroborated by the present result for the hot coaxial jet where the temperature gradient also does strengthen the acoustic radiation at higher angles.

A further analysis of the acoustic fields of the cold and hot coaxial jets is based on the power spectral density distributions in Figs. 15(a) and (b) which are obtained by the Lamb vector fluctuations. The comparison of cross-spectral density distributions shows that the additional spectral peaks are located at the Strouhal number $fD/U_s = 0.5$ of the hot coaxial jet. However, the corresponding phase velocity is lower than the sonic speed $M_c < 1$, where the acoustic radiation shows very poor efficiency. Beyond the sonic speed $M_c > 1$ both spectra show no significant difference. In other words, the

vortex sound source cannot capture the heat impact on the acoustic radiation. This cross-spectral density discussion evidences the overall sound distribution shown in Fig. 12.

3.2.2. Analysis of the entropy sources

Next, the sound generation of the hot coaxial jet is investigated in detail with respect to the impact of the temperature gradient. Based on the entropy source terms in the APE-4 system the present spectral analyses focus on the decomposed acoustic components excited by the hot primary stream. Using Eqs. (4) and (5) the entropy source terms are denoted by

$$\mathbf{q}_{e,m} = T'\nabla\overline{s} - s'\nabla\overline{T}, \tag{8}$$

$$q_{e,c} = \frac{\overline{\rho}\,\overline{a}^2}{c_p}\frac{\overline{D}s'}{Dt}. \tag{9}$$

Due to the strong temperature gradient in the radial direction the axial and azimuthal components of $\mathbf{q}_{e,m}$ have insignificant acoustic contributions. Therefore, only the radial component denoted by $q_{e,m}$ is analyzed in the following.

In Fig. 16 the instantaneous entropy source contours of the hot coaxial jet are presented. Initiated by the temperature gradient in the primary shear layer, the perturbed entropy component forms a highly intensified region surrounding the jet potential core in Fig. 16(a). The contribution of the entropy source term $q_{e,m}$ extends into the streamwise direction up to $z \simeq 12R_s$. The substantial time derivative of the perturbed entropy $q_{e,c}$ shows a pronounced turbulent mixing at the end of the jet potential core in Fig. 16(b). The acoustic oscillations in the primary shear layer have a length scale of approximately $2.5R_s$, which coincides with the wavenumber of the additional phase peak in Fig. 15(b).

In Fig. 17 the spectral density distributions are shown at several radii, i.e., at $r = 0.2R_p$, $0.6R_p$, and R_p, i.e., in the primary shear layer. Based on the same procedure used for the Lamb vector fluctuations two power spectral densities $\Phi_{e,m}$ from the radial component of entropy source $q_{e,m}$ and $\Phi_{e,c}$ from $q_{e,c}$ are defined. The left column contains the PSD of the thermal perturbation over the mean temperature gradient $q_{e,m}$, i.e., the momentum entropy, and the right column shows the PSD of the substantial time derivative of the perturbed entropy $q_{e,c}$, i.e., the continuity entropy.

Near the jet centerline the entropy sources are generated at the end of the potential core (Figs. 17(a) and (d)). It is known in Figs. 17(b) and (e) that in the hot primary jet the heat effect also generates low frequency acoustics. Due to the large temperature gradient in the primary shear layer, a high PSD value is observed at a frequency $fD_s/U_s = 0.5$ at a radius $r = R_p$ for the momentum and continuity entropy. This peak value occurs at the upstream of the end of the potential core (Figs. 17(c) and (f)). Above the primary shear layer, i.e., at the radial locations $r > R_p$, the source intensity is almost negligible. The effective source for the low frequency acoustics closely concentrates on the interior of the primary jet. The entropy sources at a frequency $fD_s/U_s = 0.5$ generate the most powerful acoustics near the primary shear layer where the strong temperature gradient intensifies the noise. The low frequency components below the frequency range $fD_s/U_s \leq 0.3$ seem to be enclosed by the strong shear layer oscillations.

In Fig. 18 contours of the root-mean-square values of the momentum entropy $\overline{q_{e,m}^2}$ and the continuity entropy $\overline{q_{e,c}^2}$ and the peak locations of the power spectral density of the entropy source spectra are shown. The local maxima of the entropy source terms are determined using the same procedure as for the Lamb vector fluctuations in Fig. 10. That is, the vanishing

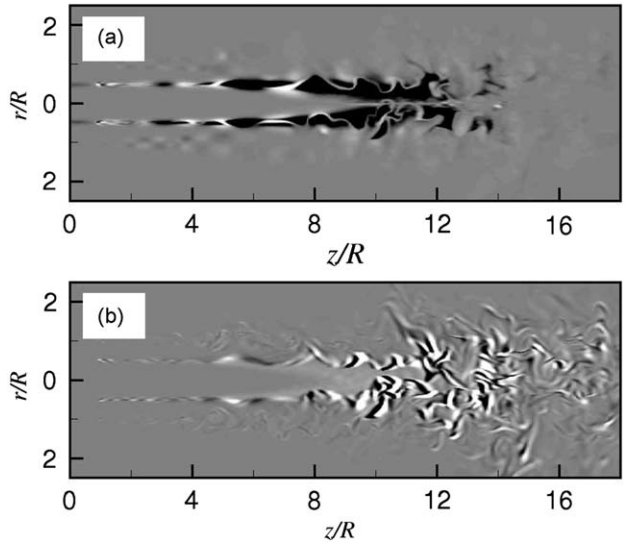

Fig. 16. Contours of the instantaneous entropy sources of the hot coaxial jet, (a) the r-component of the entropy source term of Eq. (8), $T'\partial\overline{s}/\partial r - s'\partial\overline{T}/\partial r$, in the interval $[\pm 0.05a_\infty^2/R_s]$, (b) the entropy source of Eq. (9), $(\overline{\rho}\,\overline{a^2}/c_p)\overline{D}s'/Dt$, in the interval $[\pm 0.5\rho_\infty a_\infty^3/R_s]$.

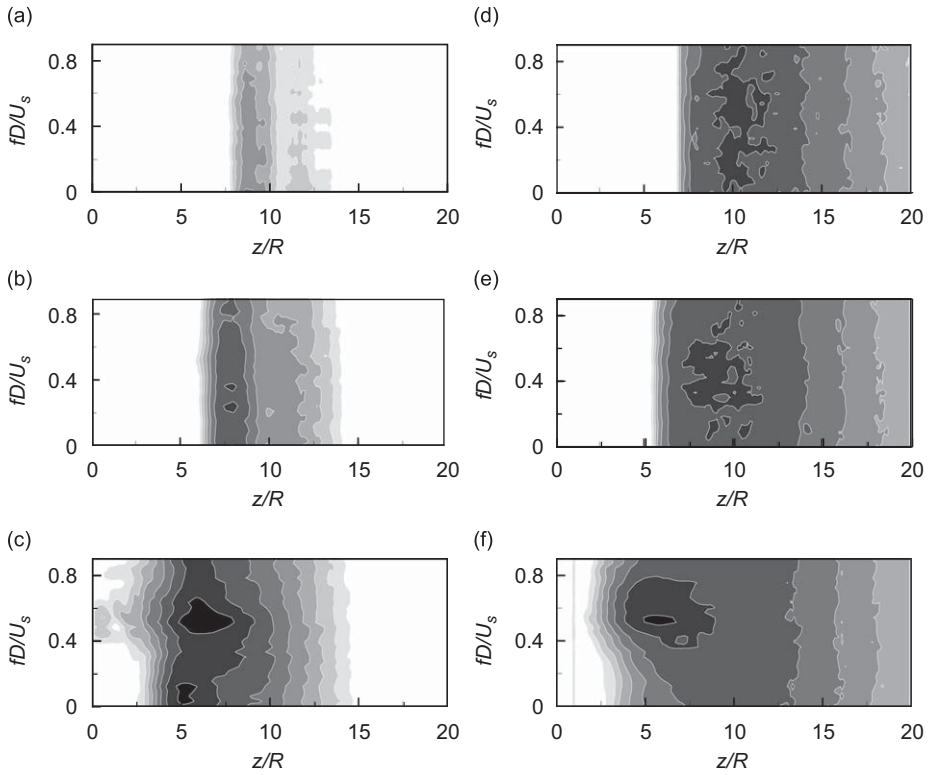

Fig. 17. Power spectral density (PSD) of the entropy sources in the hot coaxial jet at several radii, (a) and (d) at $r = 0.2R_p$, (b) and (e) at $r = 0.6R_p$, (c) and (f) at $r = R_p$; (a)–(c) $\Phi_{e,m}(f,z)$ from the entropy source term of Eq. (8), (d)–(e) $\Phi_{e,c}(f,z)$ from the entropy source term of Eq. (9), the contours are presented with eight levels in the interval $[-4 \leq \log_{10}\Phi_e \leq -1]$.

spatial gradients of $\partial\overline{q_{e,m}^2}/\partial r$ and $\partial\overline{q_{e,c}^2}/\partial r$ determine the locations of the maxima. The maximum value of the momentum entropy appears in the primary shear layer at an axial location of approximately $z \simeq 5R_s$ near the envelope of the primary potential core as shown in Fig. 18(a). The pronounced temperature gradient in the primary shear layer excites the nonlinear development of the shear layer instability which initiates the strong aeroacoustic oscillations. The maxima of the momentum entropy occur on two curves. One curve is more parallel to the streamwise direction and the other curve follows the envelope of the potential core of the primary jet, i.e., it is cone-shaped as the vortex sound core. Compared with the distributions of the maxima of the momentum entropy $q_{e,m}$ the continuity entropy $q_{e,c}$ shows in Fig. 18(b) only one cone-shape curve which is more elongated in the streamwise direction.

Considering the curves of the maxima location the acoustic core can be identified near the potential core. By illustrating the maxima curves and the spectral peak positions, such an acoustic core identification is shown in Fig. 18(c). The spectral peaks outside the primary shear layer have a negligible acoustic contribution. The strongest spectral peaks are located near the primary shear layer. The acoustics of these components determine the downstream sound field. The observed spectral peaks along the acoustic core define the locations of the major sound generation mechanism in hot coaxial jets. As has been shown before, the main characteristics of the sound field of a coaxial jet is the aeroacoustic oscillation excited by the pronounced temperature gradient and the low frequency noise induced by the heated isotropic turbulence.

4. Conclusion

The flow field and the acoustic field of one single jet and two coaxial jet configurations, one cold and one hot coaxial jet, have been analyzed. The Reynolds number $Re = 400,000$ and the Mach number $M = 0.9$ of the single and coaxial jets were alike. For the coaxial jets the reference velocity and length scale were the velocity of the secondary jet and the diameter of the nozzle exit. The primary jet temperature of the cold coaxial configuration was the ambient temperature $T_p = T_\infty$, whereas that of the hot coaxial jet is defined by $T_p = 2.7T_\infty$. The main objective of the analysis was to understand the differences between single and coaxial jets and the impact of the temperature gradient on the acoustic field.

The numerical method was based on a hybrid LES/APE method, i.e., first the flow field was computed by a large-eddy simulation and then the acoustic field was determined by solving the acoustic perturbation equations in the APE-4 form.

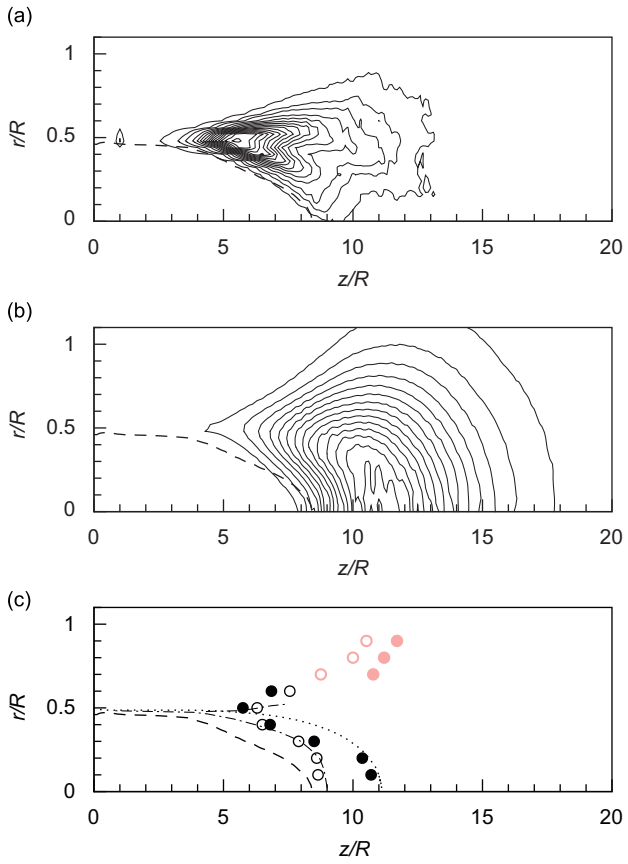

Fig. 18. Contours of the momentum and continuity entropy source terms of Eqs. (8) and (9) and the peak locations of power spectral density in the hot coaxial jet, (a) $\overline{q_{e,m}^2}$, (b) $\overline{q_{e,c}^2}$, (c) spectral peak: – – – the surface of the potential core of the primary jet, – · – the maxima of $\overline{q_{e,m}^2}$ contours, · · · the maxima of $\overline{q_{e,c}^2}$ contours, ◦ the spectral peak of $\Phi_{e,m}(f,z)$, • the spectral peak of $\Phi_{e,c}(f,z)$.

The acoustic source terms consist of the Lamb vector fluctuations ($\mathbf{L}'$), the entropy source terms ($\mathbf{q}_{e,m}$ and $\mathbf{q}_{e,c}$), and the nonlinear source terms $\nabla\cdot(\rho'\mathbf{u}')'$ in Eq. (4) and $(\nabla(u')^2/2)'$ in Eq. (5).

Considering the flow field the single jet and the cold coaxial jet show almost an identical distribution of the mean velocity and the turbulence intensity. The strong temperature gradient in the hot coaxial jet enhances the mixing resulting in a steep increase of the turbulence intensity distribution near the end of the potential core which moves clearly upstream compared with the single jet and the cold coaxial jet distributions.

The overall acoustics and the corresponding sound spectra based on the hybrid LES/APE approach are in convincing agreement with the direct LES-based acoustics solution. The analysis of the single jet shows the peak locations of the power spectral density of the Lamb vector fluctuations to define the noise generation location which possesses a cone-like shape similar to that of the potential core.

The sound generation in the coaxial jets is characterized by two features. The first feature is the downstream acoustics due to the large scale turbulence at the end of the jet potential core and the second one is the sideline acoustics enhanced by the temperature gradient, i.e., the low frequency sound is increased by up to 5 dB. According to the analytical solution of Lighthill's acoustic analogy this low frequency is dipole sound due to isotopic turbulence being intensified by the temperature gradient. Furthermore, the mean temperature difference between the primary and secondary jet causes a distinct acoustic radiation at $\theta = 35^\circ$ from the jet axis. Note that the findings cannot be immediately generalized to a single jet or a coaxial jet configuration with an inverted-velocity profile.

Using Fourier analysis for the hot coaxial jet, the spectral density distributions show the entropy sources to form a cone-like surface being wrapped around the end of the potential core. The acoustic core being characterized by the entropy source terms generates low frequency dipole sound and enhances the downstream acoustics.

References

[1] M.J. Lighthill, On sound generated aeroacoustically: I. General theory, *Proc. R. Soc. London Ser. A* 211 (1952) 564–587.
[2] M.J. Lighthill, On sound generated aeroacoustically: II. Turbulence as a source of sound, *Proc. R. Soc. London Ser. A* 222 (1954) 1–32.

[3] C.K.W. Tam, Jet noise: since 1952, *Theor. Comput. Fluid Dyn.* 10 (1998) 393–405.
[4] I. Proudman, The generation of noise by isotropic turbulence, *Proc. R. Soc. London Ser. A* 214 (1952) 119–132.
[5] G.M. Lilley, On the noise from air jets, *AGARD CP 131*, 1973, pp. 13.1–13.12.
[6] B.J. Tester, C.L. Morfey, Developments in jet noise modelling—theoretical predictions and comparisons with measured data, *J. Sound Vib.* 46 (1) (1976) 79–103.
[7] J. Laufer, R. Schlinker, R.E. Kaplan, Experiments on supersonic jet noise, *AIAA J.* 14 (4) (1976) 489–497.
[8] J. Panda, R.G. Seasholtz, Experimental investigation of density fluctuations in high-speed jets and correlation with generated noise, *J. Fluid Mech.* 450 (2002) 97–130.
[9] K. Viswanathan, Aeroacoustics of hot jets, *J. Fluid Mech.* 516 (2004) 39–82.
[10] C.K.W. Tam, K. Viswanathan, K.K. Ahuja, J. Panda, The sources of jet noise: experimental evidence, *J. Fluid Mech.* 615 (2008) 253–292.
[11] J.B. Freund, Noise sources in a low-Reynolds-number turbulent jet at Mach 0.9, *J. Fluid Mech.* 438 (2001) 277–305.
[12] C. Bogey, C. Bailly, Direct computation of the sound radiated by a high Reynolds number, subsonic round Jet, *CEAS Workshop from CFD to CAA*, November 2002.
[13] P.R. Spalart, M.L. Shur, M.Kh. Strelets, Identification of sound sources in large-eddy simulations of jets, AIAA Paper 2007-3616, 2007.
[14] J.E. Ffowcs-Williams, The noise from turbulence convected at high speed, *Trans. R. Soc. London Ser. A* 255 (1061) (1963) 469–503.
[15] A. Powell, Theory of vortex sound, *J. Acoust. Soc. Am.* 36 (1964) 177–195.
[16] C.L. Morfey, B.J. Tester, Noise measurements in a free jet flight simulation facility: shear layer refraction and facility-to-flight corrections, *J. Sound Vib.* 54 (1) (1977) 83–106.
[17] H.K. Tanna, Coannular jets—are they really quiet and why?, *J. Sound Vib.* 72 (1) (1980) 97–118.
[18] H.K. Tanna, P.J. Morris, The noise from normal-velocity-profile coannular jets, *J. Sound Vib.* 98 (1) (1985) 213–234.
[19] M.D. Dahl, D. Papamoschou, Analytical predictions and measurements of the noise radiated from supersonic coaxial jets, *AIAA J.* 38 (4) (2000) 584–591.
[20] K. Viswanathan, Parametric study of noise from dual-stream nozzles, *J. Fluid Mech.* 521 (2004) 35–68.
[21] C.K.W. Tam, N.N. Pastouchenko, K. Viswanathan, Broadband shock-cell noise from dual stream jets, *J. Sound Vib.* 324 (3–5) (2009) 861–891.
[22] M.D. Dahl, P.J. Morris, Noise from supersonic coaxial jets, part 1: mean flow predictions, *J. Sound Vib.* 200 (5) (1997) 643–663.
[23] N.W.M. Ko, A.S.H. Kwan, The initial region of subsonic coaxial jets, *J. Fluid Mech.* 73 (1976) 305–332.
[24] M.J. Fisher, G.A. Preston, W.D. Bryce, A modeling of the noise from simple coaxial jets, part I: with unheated primary flow, *J. Sound Vib.* 209 (3) (1998) 385–403.
[25] B.J. Cocking, An experimental study of coaxial jet noise, N.G.T.E. Report No. 333, 1976.
[26] M.J. Fisher, G.A. Preston, C.J. Mead, A modeling of the noise from simple coaxial jets, part II: with heated primary flow, *J. Sound Vib.* 209 (3) (1998) 405–417.
[27] M.D. Dahl, P.J. Morris, Noise from supersonic coaxial jets, part 2: normal velocity profile, *J. Sound Vib.* 200 (5) (1997) 665–699.
[28] E. Murakami, D. Papamoschou, Mean flow development in dual-stream compressible jets, *AIAA J.* 40 (6) (2002) 1131–1138.
[29] M.L. Shur, P.R. Spalart, M.Kh. Strelets, Noise prediction for increasingly complex jets. Part I: methods and tests, *Int. J. Aeroacout.* 4 (3–4) (2005) 213–246.
[30] D. Papamoschou, Acoustic simulation of coaxial hot air jets using cold helium-air mixture jets, *J. Propul. Power* 23 (2) (2007) 375–381.
[31] N. Andersson, L.E. Eriksson, L. Davidson, LES prediction of flow and acoustical field of a coaxial jet, AIAA Paper 2005-2884, 2005.
[32] C.E. Tinney, P. Jordan, The near pressure field of co-axial subsonic jets, *J. Fluid Mech.* 611 (2008) 175–204.
[33] E. Gröschel, P. Renze, W. Schröder, M. Meinke, Towards noise reduction of coaxial jets, AIAA Paper 2007-3646, 2007.
[34] C. Bogey, S. Barré, C. Bailly, Direct computation of the noise generated by a hot coaxial jet, AIAA Paper 2007-3587, 2007.
[35] C. Fureby, F. Grinstein, Monotonically integrated large eddy simulation of free shear flows, *AIAA J.* 37 (1999) 544–556.
[36] F. Rütten, W. Schröder, M. Meinke, Large-eddy simulation of low frequency oscillations of the Dean vortices in turbulent pipe bend flows, *Phys. Fluids* 17 (3) (2005) 035107.
[37] P. Renze, W. Schröder, M. Meinke, Large-eddy simulation of film cooling flows at density gradients, *Int. J. Heat Fluid Flow* 29 (1) (2008) 18–34.
[38] E. Gröschel, Schröder, P. Renze, M. Meinke, P. Comte, Noise prediction for a turbulent jet using different hybrid methods, *Comput. Fluids* 37 (2008) 414–426.
[39] N. Alkishriwi, M. Meinke, W. Schröder, Large-eddy simulation of streamwise-rotating turbulent channel flow, *Comput. Fluids* 37 (7) (2008) 786–792.
[40] M. Meinke, W. Schröder, E. Krause, T. Rister, A comparison of second- and sixth-order methods for large-eddy simulations, *Comput. Fluids* 31 (2002) 695–718.
[41] R. Ewert, W. Schröder, Acoustic perturbation equations based on flow decomposition via source filtering, *J. Comput. Phys.* 188 (2003) 365–398.
[42] J. Freund, A proposed inflow/outflow boundary condition for direct computation of aerodynamic sound, *AIAA J.* 35 (4) (1997) 740–742.
[43] C.K.W. Tam, J.C. Webb, Dispersion-relation-preserving finite difference schemes for computational acoustics, *J. Comput. Phys.* 107 (1993) 262–281.
[44] F.Q. Hu, M.Y. Hussaini, J.L. Manthey, Low-dissipation and low-dispersion Runge–Kutta schemes for computational acoustics, *J. Comput. Phys.* 124 (1996) 177–191.
[45] W. Schröder, R. Ewert, LES-CAA coupling, in: *Large-Eddy Simulations for Acoustics*, Cambridge University Press, Cambridge, 2005.
[46] W. Schröder, R. Ewert, T.P. Bui, E. Gröschel, An LES-APE approach in computational aeroacoustics theory and applications, *VKI Lecture Note VKI-LS 2006-05*, 2006.
[47] E. Gröschel, M. Meinke, W. Schröder, Noise prediction for a turbulent jet using an LES/CAA method, AIAA Paper 2005-3039, 2005.
[48] S.R. Koh, E. Gröschel, M. Meinke, W. Schröder, Numerical analysis of sound sources in high Reynolds number single jets, AIAA Paper 2007-3591, 2007.
[49] B.J. Boersma, G. Brethouwer, F.T.M. Nieuwstadt, A numerical investigation on the effect of the inflow conditions on the self-similar region of a round jet, *Phys. Fluids* 10 (4) (1998) 899–909.
[50] C. Bogey, C. Bailly, Effects of inflow conditions and forcing on subsonic jet flows and noise, *AIAA J.* 43 (5) (2005) 1000–1007.
[51] K.B.M.Q. Zaman, Flow field and near and far sound field of a subsonic jet, *J. Sound Vib.* 106 (1) (1986) 1–16.
[52] V.H. Arakeri, A. Krothapalli, V. Siddavaram, M.B. Alkislar, L.M. Lourenco, On the use of microjets to suppress turbulence in a Mach 0.9 axisymmetric jet, *J. Fluid Mech.* 490 (2003) 75–98.
[53] K.K. Ahuja, J. Lepicovsky, C.K.W. Tam, P.J. Morris, R.H. Burrin, Tone-Excited Jet, NASA-CR-3538, 1982.
[54] S. Barré, V. Fleury, C. Bogey, C. Bailly, D. Juvé, Experimental study of the properties of near-field and far-field jet noise, AIAA Paper 2006-2649, 2006.
[55] P.G. Tucker, Novel MILES computations for jet flows and noise, *Int. J. Heat Fluid Flow* 25 (4) (2004) 625–635.
[56] E.J. Avital, M. Alonso, V. Supontisky, Computational aeroacoustics: the low speed jet, *Aeronaut. J.* 112 (1133) (2008) 405–414.
[57] C.J. Mead, Specification of nozzle and flow conditions for CoJeN, CoJeN deliverable 0.1, Sixth Framework Programme EC Contract No. AST3-CT-2003-502790, 2004.
[58] C.L. Morfey, Amplification of aerodynamic noise by convected flow inhomogeneities, *J. Sound Vib.* 31 (4) (1973) 391–397.
[59] G.M. Lilley, The radiated noise from isotropic turbulence with application to the theory of jet noise, *J. Sound Vib.* 190 (3) (1996) 463–476.
[60] T.P. Bui, W. Schröder, Acoustic wave refraction in open turbulent flames, *Acta Acustica United with Acustica* 95 (3) (2009) 440–447.